Monthly Notices
of the
ROYAL ASTRONOMICAL SOCIETY

MNRAS **485,** 179–188 (2019)
Advance Access publication 2019 February 6

doi:10.1093/mnras/stz367

A Bayesian model for inferring properties of the local white dwarf population in astrometric and photometric surveys

Axel Widmark [1★] Daniel J. Mortlock[2,3,4] and Hiranya V. Peiris[1,5]

[1] *The Oskar Klein Centre for Cosmoparticle Physics, Department of Physics, Stockholm University, AlbaNova, SE-10691 Stockholm, Sweden*
[2] *Astrophysics Group, Imperial College London, Blackett Laboratory, Prince Consort Road, London SW7 2AZ, UK*
[3] *Department of Mathematics, Imperial College London, London SW7 2AZ, UK*
[4] *Department of Astronomy, Stockholm University, AlbaNova, SE-10691 Stockholm, Sweden*
[5] *Department of Physics and Astronomy, University College London, Gower Street, London WC1E 6BT, UK*

Accepted 2019 February 4. Received 2019 February 4; in original form 2018 August 10

ABSTRACT

The *Gaia* mission is providing precise astrometry for an unprecedented number of white dwarfs (WDs), encoding information on stellar evolution, Type Ia supernovae progenitor scenarios, and the star formation and dynamical history of the Milky Way. With such a large data set, it is possible to infer properties of the WD population using only astrometric and photometric informations. We demonstrate a framework to accomplish this using a mock data set with Sloan Digital Sky Survey *ugriz* photometry and *Gaia* astrometric information. Our technique utilizes a Bayesian hierarchical model for inferring properties of a WD population while also taking into account all observational errors of individual objects, as well as selection and incompleteness effects. We demonstrate that photometry alone can constrain the WD population's distributions of temperature, surface gravity, and atmospheric composition, and that astrometric information significantly improves determination of the WD surface gravity distribution. We also discuss the possibility of identifying unresolved binary WDs using only photometric and astrometric informations.

Key words: astrometry – stars: statistics – white dwarfs.

1 INTRODUCTION

White dwarfs (WDs) are the remnants of stars with initial masses $\lesssim$ 8–10 $M_\odot$ (Ritossa, Garcia-Berro & Iben 1996; Smartt et al. 2009). The local WD population carries information about the Galaxy's star formation and dynamical history, and constrains models of stellar evolution (Winget et al. 1987; García-Berro & Oswalt 2016; El-Badry, Rix & Weisz 2018).

The Sloan Digital Sky Survey (SDSS) have observed roughly 35 000 spectroscopically confirmed WDs (Kleinman et al. 2013; Kepler et al. 2015, 2016). A fundamental difficulty in studying WDs is that their mass is degenerate with distance. This degeneracy can be broken with high-quality spectrometry and accurate atmospheric models. The *Gaia* mission, which recently published its second data release (DR2), is expected to increase the number of known WDs by approximately an order of magnitude (Jordan 2007; Carrasco et al. 2014); Jiménez-Esteban et al. (2018) and Gentile Fusillo et al. (2019) have recently published WD catalogues, the latter containing 260 000 high-confidence WDs. *Gaia* also provides astrometric information for local neighborhood WDs (Kilic et al. 2018; Hollands et al. 2018). For comparison, the astrometric mission *Hipparcos* had a limiting apparent magnitude of $V \sim 12.4$ (Perryman et al. 1997), while *Gaia* will see objects as faint as $G \sim 21$ (with this limit, a WD with a mass of 0.6 $M_\odot$ and effective temperature of 8000 K is seen to ∼400 pc, assuming no dust extinction).

In a model of the WD population, it is physically meaningful to divide the total population into WD sub-populations. WDs exhibit a range of phenomenological types that can be classified spectroscopically. In terms of photometry, the main classification is between hydrogen- or helium-dominated atmospheric envelopes (Tremblay & Bergeron 2008; Bergeron et al. 2011; Koester & Kepler 2015). Hydrogen- and helium-dominated WDs follow different colour tracks and can be identified with accurate photometry, as demonstrated by Harris et al. (2006), Kilic et al. (2006), and Mortlock, Peiris & Ivezic (2009). The halo WD population is kinematically warmer and older than the disc WD population, such that inferring and comparing properties of these sub-populations can yield information on the star formation and kinematic history of our Galaxy (Isern et al. 1998; Dame et al. 2016). The sub-population of binary WD systems holds information about stellar evolution (Postnov & Yungelson 2014; Toonen et al. 2017; Kilic et al. 2018) and Type Ia supernovae progenitor scenarios (Livio & Mazzali 2018), but unresolved binaries are very difficult to identify even with high-quality spectroscopy. The formation of WDs in binary

★ E-mail: axel.widmark@fysik.su.se

Table 1. The population parameters of our model, and the object parameters and data of the respective stars.

$\boldsymbol{\Psi}$	Population parameters
α	Slope of temperature distribution
β	Relative weight of the surface gravity Gaussians
$\bar{g}_{\{1,2\}}$	Means of the surface gravity Gaussians
$\sigma_{\mathrm{g},\,\{1,\,2\}}$	Widths of the surface gravity Gaussians
f_{He}	The fraction of helium-dominated type WDs
$\boldsymbol{\psi}_{i=1,\ldots,N}$	Object parameters
T	Effective temperature
g	Surface gravity
t	Atmospheric type (hydrogen or helium)
$\boldsymbol{x}$	Spatial position
$\boldsymbol{d}_{i=1,\ldots,N}$	Data
$\hat{m}_{\mathrm{b}}$	Observed photometric magnitude
σ_{b}	Magnitude uncertainty
$\hat{\varpi}$	Observed parallax
$\sigma_{\hat{\varpi}}$	Parallax uncertainty
l	Observed Galactic longitude
b	Observed Galactic latitude

systems also gives rise to a multicomponent WD mass distribution; merging WD binaries can produce heavy WDs, while stable Roche lobe overflow or common envelope evolution of close binaries can give rise to very low-mass WDs (Kleinman et al. 2013; Althaus, Miller Bertolami & Córsico 2013; Istrate et al. 2016; Li et al. 2018).

With the enormous size of the *Gaia* data set, there is great potential for inferring properties of the WD population using photometry and astrometry, rather than the smaller data set of spectroscopically observed WDs. In this work, we demonstrate how to infer properties of the WD population in the solar neighborhood, using SDSS *ugriz* photometry and *Gaia* astrometry. We generate a mock data sample of WDs from a population model of temperature, surface gravity, and spatial number density distribution, of hydrogen and helium atmospheric types. All sample objects have photometry and parallax information with observational errors expected from SDSS and *Gaia*, and sample construction selection effects are taken into account. We also discuss the possibility of identifying binary WD systems and demonstrate how to do so using photometric and astrometric information alone.

This paper is organized as follows. We outline our model for the WD population and the observational data that we consider, in Sections 2 and 3, respectively. We present out method of statistical inference in Section 4, followed by Section 5, where we generate a mock data catalogue and infer the model parameters from that data. We discuss possible extensions to the WD model in Section 6, such as differentiating between disc and halo sub-populations, as well as the possibility of identifying unresolved double-degenerate binary WD systems. Finally, in Section 7, we present our conclusions.

2 MODEL

We model the Milky Way's population of WDs by a spatial distribution, and distributions in intrinsic WD properties. A WD is parametrized by effective temperature (T), surface gravity (g),[1] phenomenological type (t), and spatial position ($\boldsymbol{x}$). These are listed in Table 1, along with the population parameters and data.

[1]In this article, we write the surface gravity as g for shorthand, meaning $\log[g/(\mathrm{cm\,s^{-2}})]$.

There are five population parameters in our model, encapsulated in a vector $\boldsymbol{\Psi}$: the population parameter α, which parametrizing the distribution of temperatures; β, $\bar{g}$, σ_{g} which parametrize the distribution of surface gravities; and f_{He} which is the fraction of helium-dominated WDs.

The distribution of effective temperature is parametrized as

$$\Pr(T|\boldsymbol{\Psi}) \propto \Theta(T - T_{\mathrm{min}})\,\Theta(T_{\mathrm{max}} - T)\,\exp(-\alpha T), \tag{1}$$

where Θ is the Heaviside step function, and $T_{\mathrm{min}} = 5000$ K and $T_{\mathrm{max}} = 120\,000$ K the lower and upper bounds on the effective temperature. The upper and lower bounds to the effective temperature are not seen due to selection effects, as we shall see in Section 5.1. Thus, our model is not sensitive to the exact values of these bounds.

The distribution of surface gravity is parametrized by a sum of two Gaussians, according to

$$\Pr(g|\boldsymbol{\Psi}) \propto \beta\mathcal{N}(g|\bar{g}_1, \sigma_{\mathrm{g},1}) + (1-\beta)\mathcal{N}(g|\bar{g}_2, \sigma_{\mathrm{g},2}), \tag{2}$$

where β correspond to the relative weights of the Gaussians, $\bar{g}_{\{1,2\}}$ are the means, and $\sigma_{\mathrm{g},\,\{1,\,2\}}$ are the widths. This can account for possible multimodality in the surface gravity distribution (although in this case only two separate modes).

The type of the object constitutes a third parameter of the intrinsic WD properties, called t. This is a label, denoting for example if the WD is of hydrogen or helium atmospheric classification. The probabilities are written in terms of the fraction of helium WDs, as

$$\begin{aligned}\Pr(t = \mathrm{H}|\boldsymbol{\Psi}) &= (1 - f_{\mathrm{He}}),\\ \Pr(t = \mathrm{He}|\boldsymbol{\Psi}) &= f_{\mathrm{He}}.\end{aligned} \tag{3}$$

Given the intrinsic properties of a WD, the absolute magnitude in different photometric bands can be calculated using a stellar model. In this paper, we use the Bergeron atmospheric models for WDs (Bergeron, Wesemael & Beauchamp 1995; Finley, Koester & Basri 1997; Bergeron, Leggett & Ruiz 2001; Fontaine, Brassard & Bergeron 2001).

Also included in our model is a WD number density function, based on a Galactic model by Jurić et al. (2008), expressed in terms of cylindrical coordinates R, Z, and Φ:

$$\begin{aligned}n(\boldsymbol{x}) \propto \Bigg\{ &\exp\left(-\frac{R}{L_{\mathrm{thin}}}\right)\exp\left(-\frac{|Z|}{H_{\mathrm{thin}}}\right)\\ &+ f_{\mathrm{thick}}\exp\left(-\frac{R}{L_{\mathrm{thick}}}\right)\exp\left(-\frac{|Z|}{H_{\mathrm{thick}}}\right)\\ &+ f_{\mathrm{halo}}\left[\frac{(R^2 + Z^2/q_{\mathrm{halo}}^2 + R_{\mathrm{core}}^2)^{1/2}}{L_{\mathrm{halo}}}\right]^{-\eta_{\mathrm{halo}}}\Bigg\},\end{aligned} \tag{4}$$

where $f_{\mathrm{thick}} = 0.06$, $f_{\mathrm{halo}} = 6 \times 10^{-5}$, $L_{\mathrm{thin}} = L_{\mathrm{thick}} = 3.5$ kpc, $L_{\mathrm{halo}} = 8.5$ kpc, $R_{\mathrm{core}} = 1$ kpc, $H_{\mathrm{thin}} = 0.26$ kpc, $H_{\mathrm{thick}} = 1$ kpc, $q_{\mathrm{halo}} = 0.64$, and $\eta_{\mathrm{halo}} = 2$. Assuming a solar position of $R_{\odot} = 8$ kpc (where the height of the Sun above the plane is neglected), the Galactic coordinates are given by cylindrical heliocentric coordinates through

$$\begin{aligned}R(d, l, b) &= (d^2\cos^2 b - 2R_{\odot}d\cos^2 b\cos^2 + R_{\odot}^2)^{1/2},\\ Z(d, l, b) &= d\sin b.\end{aligned} \tag{5}$$

The azimuthal angle can be neglected, as the Galaxy is assumed to be axisymmetric in this model.

3 DATA

The data for a given WD are apparent magnitude measurements in photometric bands ($\hat{m}_{\mathrm{b}}$), a parallax measurement ($\hat{\varpi}$), angular

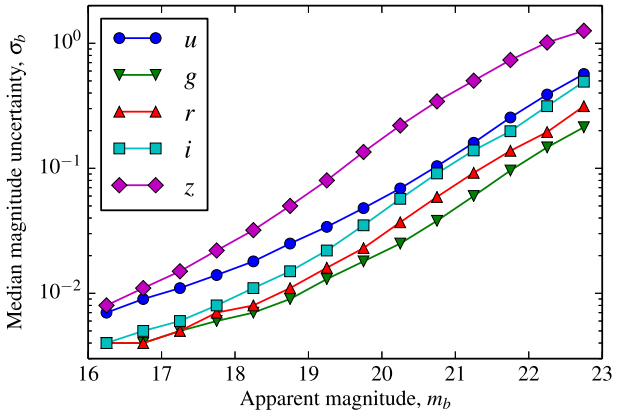

Figure 1. Median magnitude uncertainties for photometric bands $b = \{u, g, r, i, z\}$ in SDSS DR9, as a function of observed apparent magnitude. This is described in greater detail in Section 3.

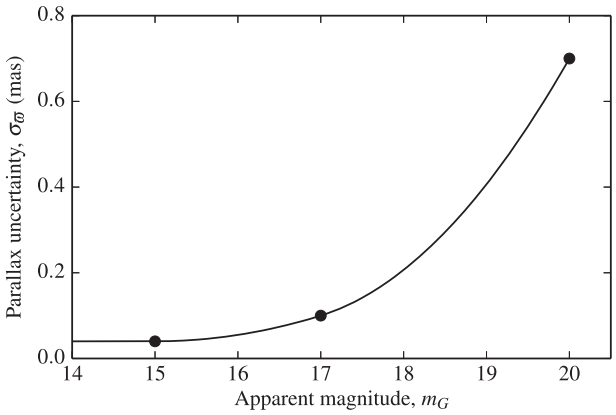

Figure 2. Parallax uncertainties as a function of *Gaia* G-band apparent magnitude m_G. The dots correspond to magnitudes $m_G = \{15, 17, 20\}$. For $m_G \leq 15$, the parallax uncertainty is 0.04 mas and constant. At higher m_G, the dots are interpolated using a second-order polynomial spline.

positions (l and b), including the error models of these observables.[2] The data characterizing a WD with index i, called $\boldsymbol{d}_i$, is listed in Table 1.

The contribution to the likelihood from the data in the each photometric band is calculated in flux instead of magnitudes, which is important for objects with a low signal-to-noise ratio where a first-order error propagation from flux to magnitude is inaccurate. The likelihood associated with a WD is

$$\Pr(\boldsymbol{d}_i|\boldsymbol{\psi}_i) = \mathcal{N}(\varpi(\boldsymbol{\psi}_i)|\hat{\varpi}, \sigma_{\hat{\varpi}}) \prod_b \mathcal{N}(F_b(\boldsymbol{\psi}_i)|\hat{F}_b, \sigma_{F,b}), \tag{6}$$

where $\mathcal{N}(x|\mu, \sigma)$ is the normal distribution of mean μ and standard deviation σ, $F_b(\boldsymbol{\psi}_i)$ is the true flux as given by the object parameters, and $\hat{F}_b$ is the observed flux with uncertainty $\sigma_{F,b}$. The conversions between fluxes and magnitudes are as given in appendix 2A in Mortlock et al. (2012). The factor containing parallax information is dropped when no parallax information is present.

In this work, we use SDSS photometry in *ugriz* colour bands, and a Bergeron atmospheric stellar model, as discussed in Section 2. In order to assign realistic uncertainties to the mock data that we generate, we use median uncertainties of the SDSS DR9 catalogue (Ahn et al., 2012), in bins of observed apparent magnitude of width 0.5 mag. These median uncertainties are shown in Fig. 1. We limit the minimum *ugriz* magnitude uncertainty to 0.01 mag, in order to account for possible systematic uncertainties in the Bergeron atmospheric model. In principle, the photometry of *Gaia* or other surveys could also be used in this framework. However, the *Gaia* DR2 colours are more uncertain than SDSS and potentially more prone to systematics (Evans et al. 2018); therefore we only use SDSS photometry in this work.

We use parallax information with the precision of *Gaia* DR2, which has a limiting magnitude of $m_G \simeq 21$. As listed in Lindegren et al. (2018), the parallax uncertainties of *Gaia* DR2 are about 0.04 mas for sources with $m_G < 15$, about 0.1 mas for sources with $m_G = 17$, and about 0.7 mas at $m_G = 20$. In order to account for this magnitude dependence, we interpolate these points as shown in Fig. 2. The errors in the *Gaia* photometric G band are interpolated in the same manner as for the parallax, with errors of 0.3 mmag for $m_G = 13$, 2 mmag for $m_G = 17$, and 10 mmag for $m_G = 20$. This distribution can be compared to the parallax uncertainty distribution presented in the appendix of Luri et al. (2018), which is an expected end-of-mission precision. These two distributions have minor differences at a level which would lead to a negligible effect on our results.

[2]A hatted quantity (e.g. $\hat{\varpi}$) refers to an observed value, while a non-hatted quantity (e.g. ϖ) refers to an observable's true value. The angles l and b are written without hats, as their measurement uncertainties are so small that they can be neglected.

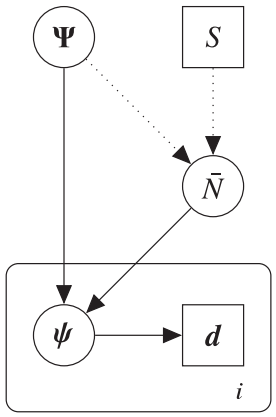

Figure 3. A DAG of our statistical model. Quantities inscribed in circles (squares) represent parameters (constants); solid (dotted) arrows represent probabilistic (deterministic) dependence; a rectangle with rounded corners represents a set of objects, in this case, the set of WD included in our sample, carrying an index i; $\boldsymbol{\Psi}$ is the set of population parameters, S is the selection function of our sample construction, $\bar{N}$ is the normalization to the WD distribution function, $\boldsymbol{\psi}$ is the set of object parameters, $\boldsymbol{d}$ is the object data, and i is the object index.

4 STATISTICAL MODEL

A directed acyclical graph (DAG) of our statistical model is shown in Fig. 3. In the DAG, the constants and parameters of the model are inscribed in squares and circles; the arrows indicate the generative relationship between these quantities.

By Bayes' Theorem, the full posterior on both population parameters and object parameters is written

$$\Pr(\boldsymbol{\Psi}, \boldsymbol{\psi}|\boldsymbol{d}) = \Pr(\boldsymbol{\Psi}) \prod_i \frac{S(\boldsymbol{d}_i)\Pr(\boldsymbol{d}_i|\boldsymbol{\psi}_i)\Pr(\boldsymbol{\psi}_i|\boldsymbol{\Psi})}{\bar{N}(S, \boldsymbol{\Psi})}, \tag{7}$$

where $\Pr(\boldsymbol{\Psi})$ is a prior on the population parameters; $S(\boldsymbol{d}_i)$ is the probability of being selected given the data of that object; $\Pr(\boldsymbol{d}_i|\boldsymbol{\psi}_i)$ is the likelihood of the data of an object given its object parameters; $\Pr(\boldsymbol{\psi}_i|\boldsymbol{\Psi})$ is the probability of object parameters given the population parameters; finally, $\bar{N}(S, \boldsymbol{\Psi})$ is the normalization of $\Pr(\boldsymbol{\psi}_i|\boldsymbol{\Psi})$, and depends on the selection function and the population parameters. When writing the data or object parameters without an index i, we refer to the complete set of objects, $\boldsymbol{\psi} \equiv \{\boldsymbol{\psi}_1, \boldsymbol{\psi}_2, \ldots, \boldsymbol{\psi}_N\}$.

4.1 Object parameters

Each WD has a set of object parameters encapsulated in $\boldsymbol{\psi}_i$, as listed in Table 1. Because the angular position errors can be neglected, the spatial position only varies in terms of the object's distance. Conceptually, the most straightforward parametrization would be to have the distance d as an object parameter. However, this creates some sampling difficulties arising from the fact that g and d are highly degenerate, especially when there is no parallax information available. In this work, we sample the object parameter posteriors using a Metropolis–Hastings Markov Chain Monte Carlo (MCMC) algorithm (Metropolis et al. 1953; Brooks et al. 2011), which is more efficient when the posterior closer to a multivariate Gaussian in shape. This can be accomplished by a coordinate transformation, as is illustrated in Fig. 4. In the lower panel, the distance is parametrized in terms of Δ, which is the relative change to the ideal distance given T and g. Let $\tilde{d}(T, g)$ be the distance that maximizes the colour factor of the magnitude likelihood, which is

$$\tilde{d} = h^{-1}\left\{\frac{\sum_b \sigma_b^{-2}[\hat{m}_c - M_c(T, g)]}{\sum_b \sigma_b^{-2}}\right\}. \quad (8)$$

The function h^{-1} is the inverse of $h(d) = 5[\log_{10}(d/\mathrm{pc}) - 1]$, the difference between apparent and absolute magnitude. In principle, this distance could instead be given by the maximum of the flux likelihood, but this is accurate enough since the high-quality photometric bands dominate. The distance parametrized by the object parameters is $d = \Delta\tilde{d}(T, g)$. It is crucial to account for the Jacobian factor that arises with this parametrization, in which the differentials are replaced according to

$$\mathrm{d}T\,\mathrm{d}g\,\mathrm{d}d \to \mathrm{d}T\,\mathrm{d}g\,\mathrm{d}\Delta\,J(T, g), \quad (9)$$

where the Jacobian is

$$J(T, g) = \tilde{d}(T, g), \quad (10)$$

which has no dependence on Δ.

4.2 Object posterior

The posterior on a specific object also includes the term $\Pr(\boldsymbol{\psi}_i|\boldsymbol{\Psi})$, normalized by the quantity $\bar{N}(S, \boldsymbol{\Psi})$. It is given by the population parametrized by

$$\begin{aligned}&\Pr(\boldsymbol{\psi}_i|\boldsymbol{\Psi})\,\mathrm{d}T\,\mathrm{d}g\,\mathrm{d}d\\ &\quad\propto d^2 n(l, b, \varpi)\Pr(T, g, t|\boldsymbol{\Psi})\,\mathrm{d}T\,\mathrm{d}g\,\mathrm{d}d\\ &\quad= \Delta^2\tilde{d}^3(T, g, t)n(l, b, \varpi)\Pr(T, g, t|\boldsymbol{\Psi})\,\mathrm{d}T\,\mathrm{d}g\,\mathrm{d}\Delta,\end{aligned} \quad (11)$$

where n is the number density of WDs as a function of spatial position. It is implicit in this expression that the true parallax ϖ is a function of the object parameters $\boldsymbol{\psi}_i$.

The normalization factor is given by an integral (or sum, in the case of a discrete variable) over the possible properties of a hypothetical WD drawn from the population model, multiplied by the probability of being selected, as

$$\bar{N}(S, \boldsymbol{\Psi}) = \sum_t \int \mathrm{d}T\,\mathrm{d}g\,\mathrm{d}^3\boldsymbol{x}\,\Pr(T, g, t|\boldsymbol{\Psi})\,n(\boldsymbol{x})\,S(T, g, t, \boldsymbol{x}). \quad (12)$$

The selection function, $S(T, g, t, \boldsymbol{x})$, is the probability of being included in the sample, given by an object's intrinsic properties and the sample construction cuts on observables.

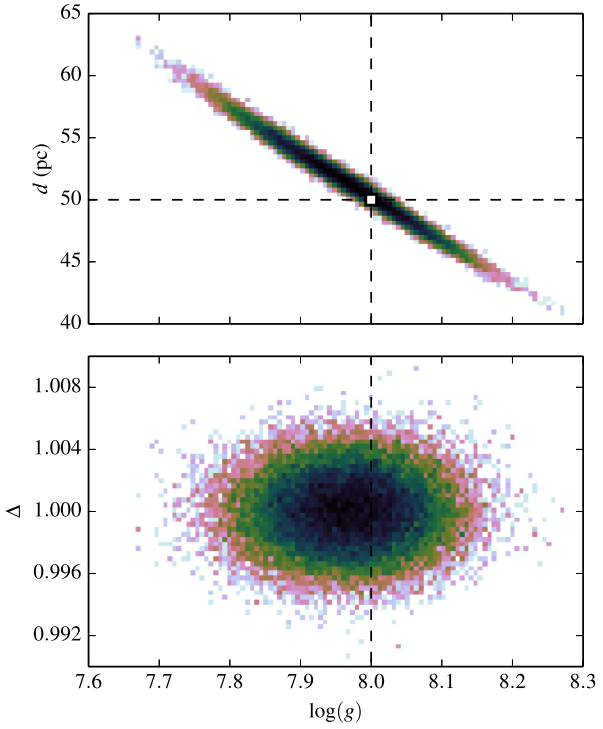

Figure 4. A posterior density of an object with true parameters $T = 14000$ K, $g = 8.0$, $t =$ DA, and $d = 50$ pc, with photometric errors of $\sigma_c = 0.01$ in all *ugriz* colour bands. The population parameters are set to $\alpha = 3.5$, $\beta = 0.6$, $\bar{g}_1 = 8.0$, $\bar{g}_2 = 8.4$, $\sigma_{g,1} = 0.1$, $\sigma_{g,2} = 0.15$, and $f_{He} = 0$. Because there is no parallax information, the constraint on the surface gravity is largely due to the prior set by the population model. The two panels show the same posterior density, sharing the surface gravity g on the horizontal axis. The top panel shows the distance d on the vertical axis, while the bottom panel shows an alternative parametrization of the distance Δ, described in Section 4.1. The true object parameter values are marked with dashed lines and a white square. The correct value for Δ varies with T, which is marginalized over in this figure; hence, there is no true value for Δ, although it should lie close to unity. While the highly degenerate posterior distribution of the top panel can lead to sampling difficulties, the alternative parametrization of the bottom panel avoids such issues.

5 MOCK DATA AND ANALYSIS

To test the algorithm, mock data are generated from the population model. While the exact values of the population parameters are of lesser importance (the main focus being the statistical method), we chose values with the following motivations.

(i) For the temperature distribution, we chose $\alpha = 3.5$. To first order, WDs cool at a rate of $\dot{T} = T^{-3.5}$, according to Mestel (1952), although numerical models differ from this cooling rate especially for cooler WDs.

(ii) For the distribution of surface gravity, we chose $\beta = 0.6$, $\bar{g}_{\{1,2\}} = \{8, 8.4\}$, and $\sigma_{g\{1,2\}} = \{0.10.15\}$. This distribution is thus

made up of two separate modes, corresponding to WDs that have evolved as singles and WDs that are the products of merged binaries, motivated by the results of (Kilic et al. 2018). The Gaussian mixture model can be extended to also include light WDs, inflating the number of population parameters. For this demonstration of the method, we use a simpler model.

(iii) For the fraction of helium-dominated WDs, we chose $f_{\rm He} = 0.1$. The fraction of DB WDs is observed to vary with temperature, but is roughly in the range of 10–20 per cent (Bergeron et al. 2011).

We compare the case of having no astrometric information, versus having parallax measurements with the precision of *Gaia* DR2.

5.1 Sample selection

We define a sample by making cuts on observable properties, in our case on mock data of a generated catalogue. Depending on the errors of these observables, these cuts correspond more or less well to cuts in the objects' intrinsic properties. We do not make a volume-limited sample by making cuts on parallax – we wish to compare with the case where astrometry is not available, hence we need to construct the sample without such information. We make cuts in observed apparent magnitude and observed colour. The cuts in colour correspond to upper and lower limits on the temperature of WDs included in our sample. The limit in apparent magnitude sets a maximum distance for a WD, as a function of temperature, surface gravity and type.

There are several reasons for not allowing very high temperatures in our samples (although the exact limit is rather arbitrary). Very hot objects are rare in terms of spatial density, but because they are seen to much greater distances they can still be numerous in a sample that is not volume-limited. How many are seen depends on the properties of the population, but this is degenerate with the assumed spatial distribution and the distribution of Galactic dust. Furthermore, with sufficiently high temperature, the peak of an object's spectrum is of shorter wavelength than the *u* band, in which case the inference on an object's temperature becomes very weak. When working with actual data, it is also necessary to identify what objects are WDs and what objects are not. With very hot, far away objects this is difficult, especially since the distance will be poorly constrained. These issues can be circumvented with good parallax measurements, enabling the construction of a volume-limited sample.

We make the following cut in colour, demanding that

$$-0.6195 < \hat{\delta}_{\rm ugr} < 0.4369, \tag{13}$$

where

$$\hat{\delta}_{\rm ugr} \equiv -0.4925\hat{m}_{\rm u} - 0.5075\hat{m}_{\rm g} + \hat{m}_{\rm r}. \tag{14}$$

Without measurement errors, this cut corresponds to limiting the temperature of a hydrogen-dominated WD to $T \in (7000, 30000)$ K; for a helium-dominated WD, the upper limit in temperature is less restrictive, as can be seen in Fig. 5.

We also make a cut in brightness, by demanding that the *Gaia* *G*-band apparent magnitude fulfills $\hat{m}_{\rm G} < 20$. In principle, this criterion could equally well have been formulated in terms of some combination of the *ugriz* apparent magnitudes.

Given these cuts on observables, the selection function is

$$S(T, g, t, \boldsymbol{x}) = \int {\rm d}\hat{m}_{\rm G}\Theta\left(20 - \hat{m}_{\rm G}\right)\mathcal{N}\left(\hat{m}_{\rm G}|m_{\rm G}, \sigma_{\rm G}\right) \times \int {\rm d}\hat{\delta}_{\rm ugr}\,\Theta\left(\hat{\delta}_{\rm ugr} - 0.6195\right)\Theta\left(0.4369 - \hat{\delta}_{\rm ugr}\right)\mathcal{N}\left(\hat{\delta}_{\rm ugr}|\delta_{\rm ugr}, \sigma_{\delta}\right), \tag{15}$$

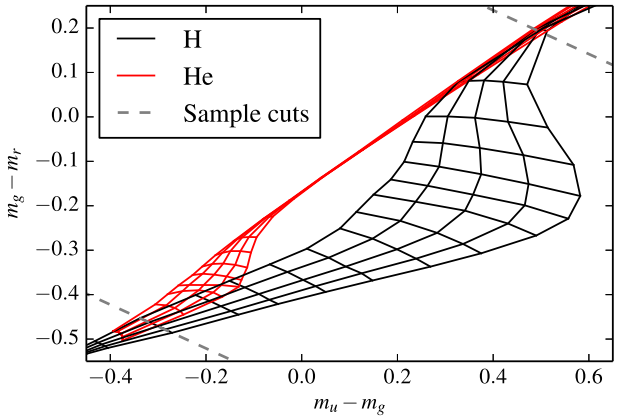

Figure 5. Colours of a hydrogen- and helium-dominated WD, in contours of constant T or g. The surface gravity takes values $g = \{7, 7.5, 8, 8.5, 9\}$. The dashed lines corresponds to the colour cuts in $\hat{\delta}_{\rm ugr}$, where only objects that fall in the region between these lines are included. Because this is a cut in observed colour, observational errors can scatter objects across the sample boundary.

where $m_{\rm G}$ and $\delta_{\rm ugr}$ are true observables with an implicit dependence on the object parameters. The error on $\hat{\delta}_{\rm ugr}$ is given by

$$\sigma_{\delta}^2 = (0.4925\sigma_u)^2 + (0.5075\sigma_g)^2 + \sigma_r^2, \tag{16}$$

assuming that the different magnitude errors are uncorrelated.

For the photometric bands that are relevant for selection (u, g, r), the uncertainties are small. When computing the normalization $\bar{N}$, see equation (12), doing so in flux or magnitude space will give the same result. The former is more expensive, which is why the selection function is written in terms of magnitudes.

5.2 Generating a mock sample

The mock sample of WDs is generated by rejection sampling. An object is drawn randomly from the true population model: the object parameters T, g, and t are distributed as described in equations (2) and (3) and can be randomized analytically; the position is distributed according to $n(\boldsymbol{x})$ and is randomized by rejection sampling, knowing that there is a maximal distance a WD can have in order to be included in our sample (observational errors included). A randomly drawn object is then assigned observable quantities, with errors as described in Section 3. If the object observables fulfille the selection cuts, the object is included in the sample; if not, it is rejected.

We construct a sample with 10^4 WDs. The distribution of true object parameter values is shown in Fig. 6, where selection effects are manifest. The maximum distance is clearly seen as a function of temperature, where hotter objects are seen further away. Due to the colour cut, the high temperature tail is more pronounced for the helium-dominated sub-population. It is also clear that low-mass WDs are more likely to be included as they are more luminous and seen to greater distances, an effect that quenches the second surface gravity mode at $g = 8.4$.

5.3 Sampling

We infer the population parameters of a Bayesian hierarchical model, as described in Section 2, for our mock data sample, using an MCMC to trace the posterior distribution. Computing the posterior value for a set of population parameters, with all

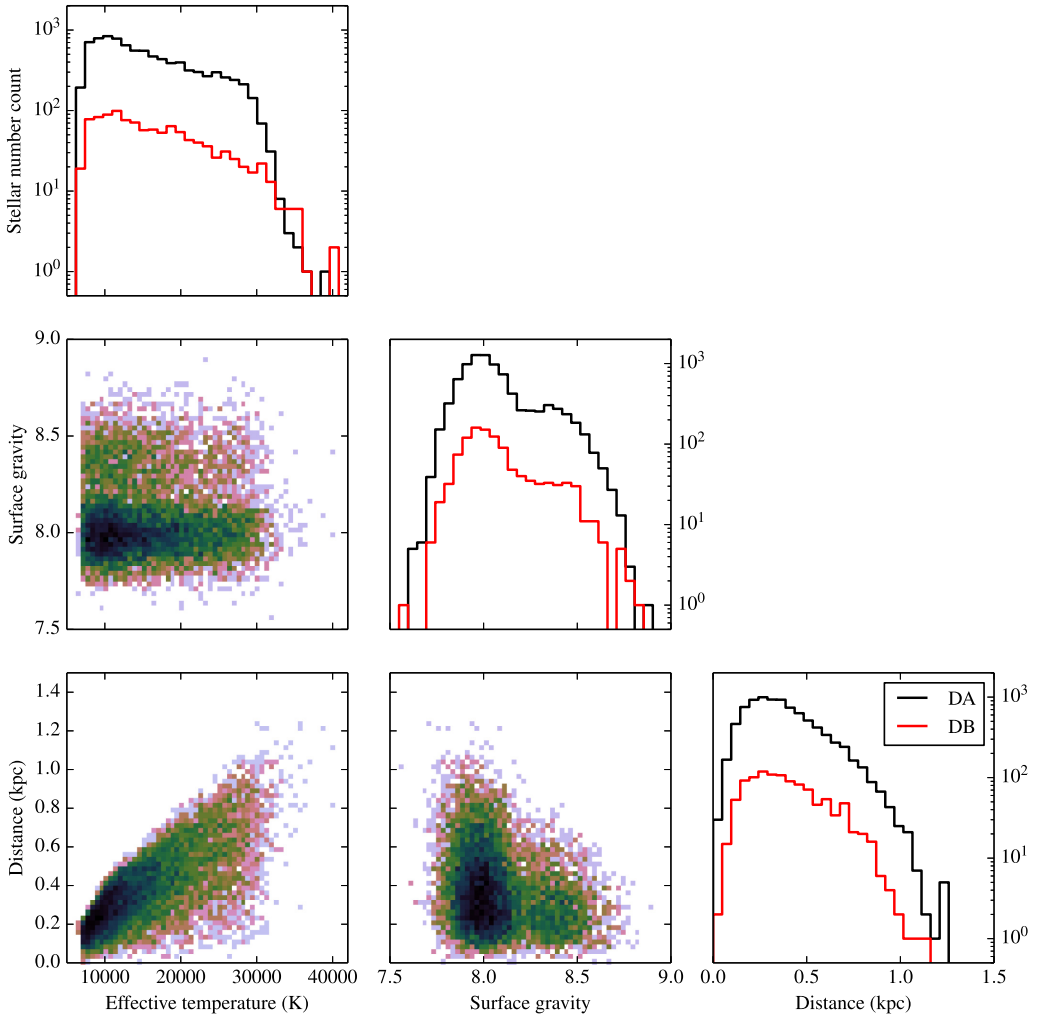

Figure 6. The distributions of true intrinsic properties of our mock data sample, represented as 1D and 2D histograms. The axis are shared between the panels, except for the vertical axis of the 1D histograms. Hydrogen- and helium-dominated WDs are plotted separately in the 1D histograms, but not in the 2D histograms.

object parameters marginalized, can be very expensive computationally due to the high number of objects. In order to be more computationally efficient, we use a special purpose sampling algorithm, where the population parameters are sampled using a standard Metropolis–Hastings MCMC (Gelman et al. 2013), but the Bayesian evidence (or marginal likelihood) of each respective WD is calculated by importance sampling. The Bayesian evidence of an object i is proportional to the integral over the object parameters,

$$\int \Pr(\boldsymbol{d}_i|\boldsymbol{\psi}_i)\Pr(\boldsymbol{\psi}_i|\boldsymbol{\Psi}). \tag{17}$$

This integral is expensive to compute, which is why it is calculated by importance sampling, which works in the following way. For each separate WD, a thinned MCMC gives a number of independently drawn points from the function in equation (17), given some background population model set by fixed population parameters. The Bayesian evidence under this background model can be computed by taking the sum of the posterior values of that chain, weighted by the volume that each point occupies; this volume weight is proportional to the nearest-neighbour distance cubed, as described in Heavens et al. (2017). The Bayesian evidence for a WD under a different set of population parameters $\boldsymbol{\Psi}$ is calculated in the same way, although the weight of each point also includes the ratio

$$\frac{\Pr(\boldsymbol{\psi}_i|\boldsymbol{\Psi})}{\Pr(\boldsymbol{\psi}_i|\boldsymbol{\Psi}_{\rm bg})}, \tag{18}$$

where $\boldsymbol{\Psi}_{\rm bg}$ is the population parameters of the background model. This is significantly cheaper computationally, as the likelihood of the data, $\Pr(\boldsymbol{d}_i|\boldsymbol{\psi}_i)$, does not need to be computed with every new step of the population parameter MCMC. The Bayesian evidence of the two WD types, hydrogen and helium dominated, are computed separately and then added together, for each respective WD.

The background model has the following population parameter values: $\alpha = 3.5$, $\beta = 1$, $\bar{g}_1 = 8.2$, $\sigma_{\rm g,\,1} = 0.3$, and $f_{\rm He} = 0.5$, thus with a surface gravity distribution consisting of only one Gaussian. It is important that the background model surface gravity distribution is similar to but wider than the inferred distribution, as it can otherwise impose artificial constraints or biases to the posterior density.

The population parameter prior, $\Pr(\boldsymbol{\Psi})$, is taken to be uniform and wide in all parameters around the true parameter values.

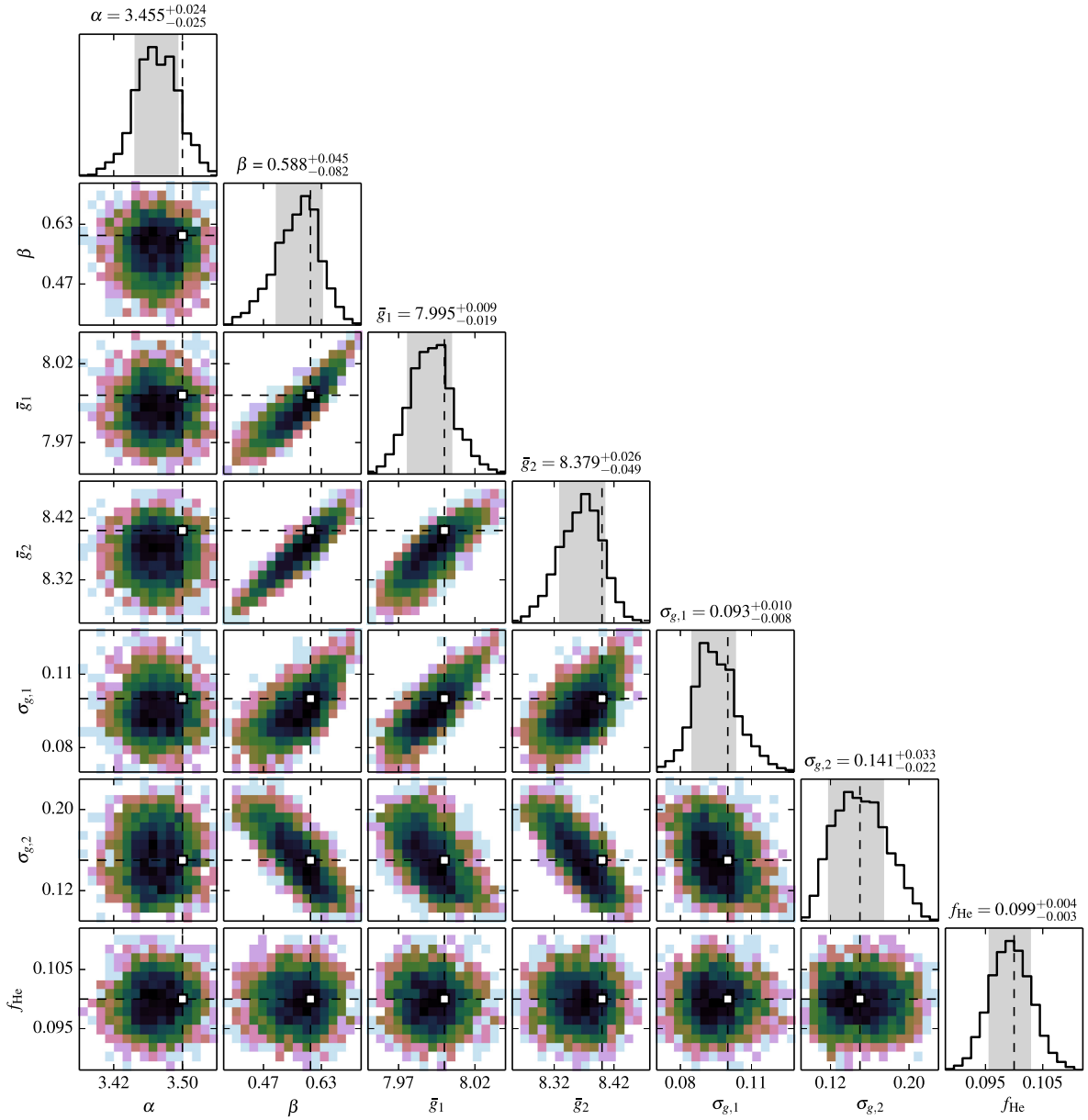

Figure 7. Posterior density of the population parameters, for a mock data set with no astrometric information. The highest posterior density (HPD) credible intervals, presented in terms of the HPD value plus/minus bounds that cover 68 per cent of the posterior density, are indicated on the panels showing 1D histograms. The true population parameter values are marked with dotted black lines, and a white square in the 2D histograms.

5.4 Results

The inferred posterior distributions are shown in Figs 7 and 8, where the former has no parallax information. In each of these chains, the Metropolis-within-Gibbs MCMC has run for 10^4 iterations.

In both cases, with and without parallax information, the correct population parameter values are recovered by the posterior distribution. When inferring the population parameters of other mock data samples (generated in the same manner), no significant biases were found. The inference on quantities α (parametrizing the distribution of effective temperature) and $f_{\rm He}$ (the fraction of helium-dominated WDs) is not significantly affected by also adding parallax information. For the remaining parameters, parametrizing the distribution of surface gravity, the inference is strongly affected when including parallax information.

6 WHITE DWARF SUB-POPULATIONS

The population of WDs in the Milky Way is richer and more complicated than the model described in Section 2. While we do consider WD sub-populations in the sense of accounting for the difference between hydrogen- and helium-dominated WDs and a simple multimodality of the surface gravity distribution, there are other meaningful ways to construct the population model. While we assume that the distribution of temperatures and surface gravities is the same between hydrogen- and helium-dominated WDs, derived from the same population parameters, it could be meaningful to have separate sets of population parameters for the two types.

In the same vein, one would expect the disc and halo WD population to have different properties. Furthermore, there is expected

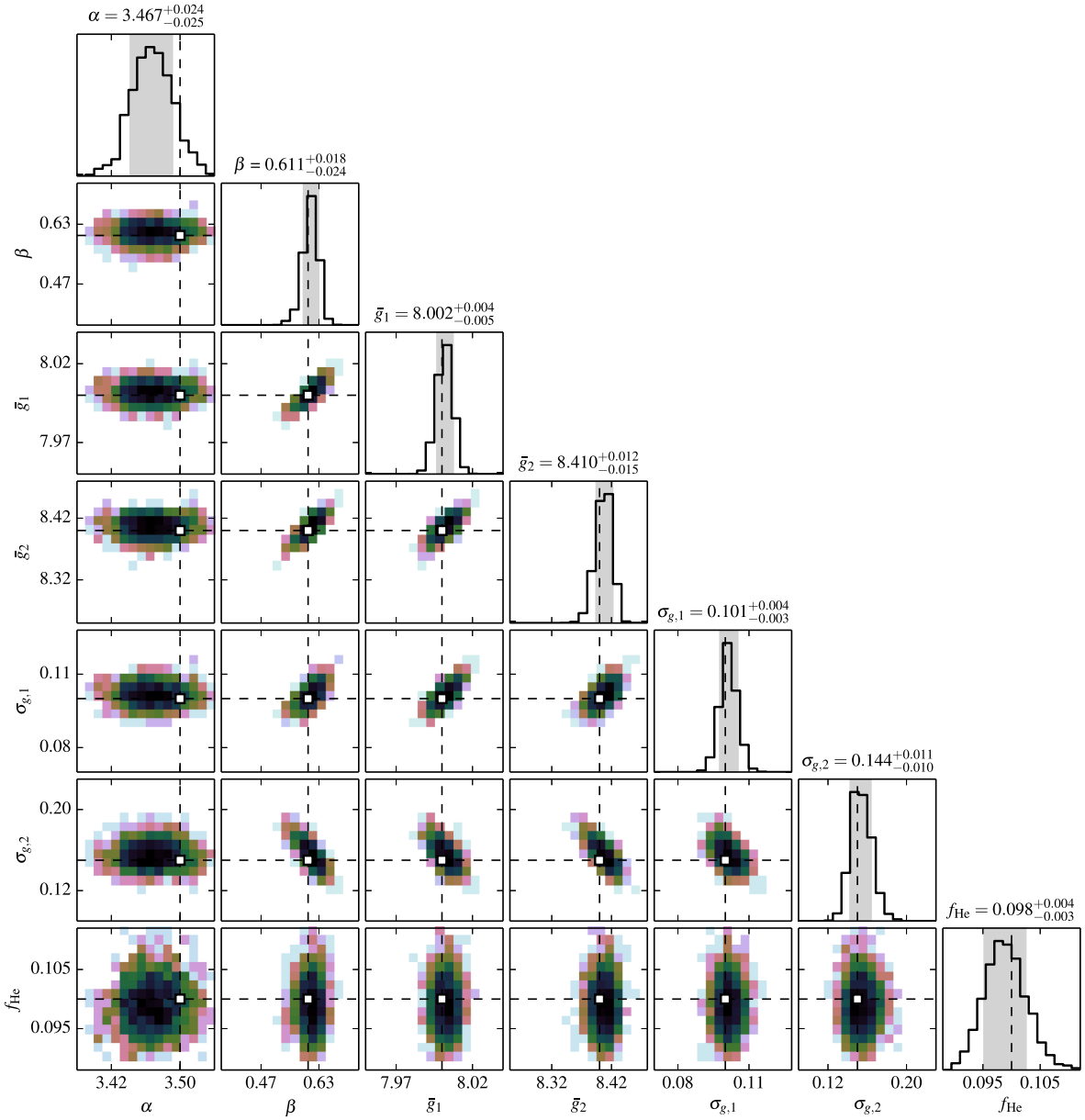

Figure 8. Posterior density of the population parameters, for a mock data set with parallax information. The HPD credible intervals, presented in terms of the HPD value plus/minus bounds that cover 68 per cent of the posterior density, are indicated on the panels showing 1D histograms. The true population parameter values are marked with dotted black lines, and a white square in the 2D histograms. The axis range of all panels are the same as in Fig. 7.

to be a sub-population of binary WD systems. We discuss how to model these two cases below.

6.1 Disc and halo populations

It would be interesting to see qualitative differences between disc and halo WDs. For example, the kinematically warmer halo population has older stars. The population of very old WDs is scientifically interesting, as it holds information about the star formation and dynamical history of the Milky Way.

In this population model, each sub-population would have its own set of population parameters: $\mathbf{\Psi} = \{\mathbf{\Psi}_{\rm disc}, \mathbf{\Psi}_{\rm halo}\}$. They would each have their respective spatial number density distributions: $n_{\rm disc}(\boldsymbol{x})$ and $n_{\rm halo}(\boldsymbol{x})$. It would be necessary to have a population parameter that describes the relative number density fraction of the two sub-populations at some reference point (e.g. the Sun's position), such that they can be normalized. The posterior, analogous to equation (7), would read

$$\Pr(\mathbf{\Psi}, \boldsymbol{\psi}|\boldsymbol{d}) = \Pr(\mathbf{\Psi}) \prod_i \frac{S(\boldsymbol{d}_{\rm i}) \Pr(\boldsymbol{d}_{\rm i}|\boldsymbol{\psi}_{\rm i}) \left[\Pr(\boldsymbol{\psi}_{\rm i}|\mathbf{\Psi}_{\rm disc}) + \Pr(\boldsymbol{\psi}_{\rm i}|\mathbf{\Psi}_{\rm halo})\right]}{\bar{N}(S, \mathbf{\Psi}_{\rm disc}, \mathbf{\Psi}_{\rm halo})}. \quad (19)$$

The total number count is simply the sum over the two sub-populations, like

$$\bar{N}(S, \mathbf{\Psi}_{\rm disc}, \mathbf{\Psi}_{\rm halo}) = \bar{N}_{\rm disc}(S, \mathbf{\Psi}_{\rm disc}) + \bar{N}_{\rm halo}(S, \mathbf{\Psi}_{\rm halo}). \quad (20)$$

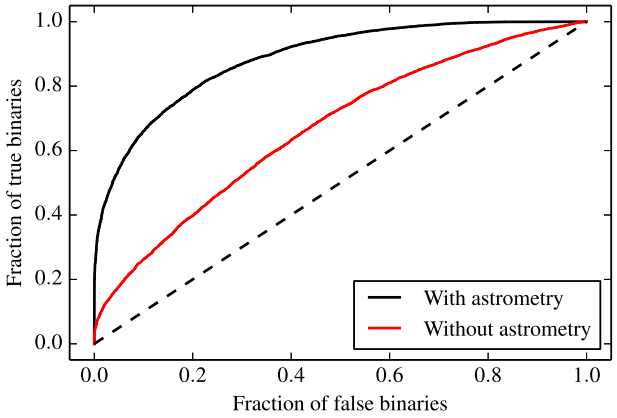

Figure 9. An ROC curve of binary WD identification. This shows the rate of falsely identified versus correctly identified binary WD systems, for the cases of having and not having parallax information. An object is labelled binary if the Bayes factor for being a binary system is above some threshold value, where this threshold value is monotonically decreasing along the graphs, from the bottom left to the top right corner of the figure. The dashed line shows the linear relationship.

6.2 Binary population

Unresolved binary WD systems can be identified using only photometry and astrometry, in a similar way to the method presented in Widmark, Leistedt & Hogg (2018). For a binary system, the likelihood is the same as in equation (6), the difference being that the *ugriz* apparent magnitudes of the two component stars are added together, according to

$$m_{\rm b,sum} = -\frac{5}{2}\log_{10}\left(10^{-\frac{2}{5}m_{\rm b,A}} + 10^{-\frac{2}{5}m_{\rm b,B}}\right), \quad (21)$$

where $m_{\rm b,\,A}$ and $m_{\rm b,\,B}$ are the b-band apparent magnitudes of the two component stars.

The posterior density of a binary system will be written in terms of seven parameters instead of four, as we have temperature, surface gravity, and type of the two component stars, and the distance of the binary system.

We construct a population of mock binaries by random pairing of the singles population and the same selection criteria, although we also add a constraint in terms of cooling time of the two component stars. In addition to the effective temperature and surface gravity distributions of the two component stars, as described by equation (2), the probability of pairing also has a factor

$$\exp\left\{-\frac{[t_{\rm cool}(T_{\rm A},\,g_{\rm A},\,t_{\rm A}) - t_{\rm cool}(T_{\rm B},\,g_{\rm B},\,t_{\rm B})]^2}{2\times(500\ {\rm Myr})^2}\right\}, \quad (22)$$

where $t_{\rm cool}(T_{\rm A},\,g_{\rm A},\,t_{\rm A})$ is the cooling time of the A component WD (and equivalently for component B), as given by the Bergeron atmospheric model. The chosen time difference of ∼500 Myr prohibits the pairing of extremely cool and faint WDs with hotter ones. This is a reasonable assumption, as binary stars are typically born in the same system and with similar properties. Without this constraint, one component star would almost always be extremely faint, making binary identification almost impossible. For reference, the cooling time of a WD with $T = 10^4$ K and $g = 7.9$ is roughly 500 Myr.

Fig. 9 shows a receiver operating characteristic (ROC) curve for identification of binaries, for the cases of having and not having parallax information. The binaries are inferred with knowledge of the underlying population model, in the sense that the population parameters are known. The Bayesian evidence for being single and binary is computed in the same way as is described in the beginning of Section 5.4. The integral is computed for all possible hydrogen/helium combinations separately, with a $T_{\rm A} > T_{\rm B}$ multiplicity constraint for binary WDs, circumventing issues of multimodal posterior densities. This is done for 10^4 mock data single WDs and 10^4 mock data binary WD systems. It is clear from Fig. 9 that binary identification is significantly improved with parallax information, for which some binaries can be strongly identified even with a very low contamination rate (20 per cent binary identification with less than 0.1 per cent contamination).

This identification is made on mock data when the underlying population model is known. Working with real data brings many complications, not least coming from the fact that the population model is unknown and inferred. Even so, this test shows that it should be possible to identify a WD binary population. An important aspect that is not accounted for here is that some WD binaries are not drawn from the same distribution of masses as the population of single WDs. A tight binary system goes through phases of mass transfer and shared envelopes; thus there will be binaries with component WD with low mass and surface gravity. Such a binary system would actually be even easier to detect using this method, as they would be brighter due to multiplicity, and brighter still from being low mass and larger in size.

7 DISCUSSION

In this paper, we demonstrate how to infer properties of the local WD population using only astrometric and photometric information, in the framework of a Bayesian hierarchical model.

In our mock sample, we have limited ourselves to a total number of 10^4 WDs and a simple population model, in order to demonstrate the statistical method. The number of high-confidence WDs in *Gaia* DR2 is already significantly higher (roughly 260 000 in Gentile Fusillo et al. 2019), although only about a tenth of them are cross-matched with SDSS. Using only *Gaia* photometry or cross-matches with other surveys for such objects, we should be able to fit a significantly more complicated model. The model could be extended with more complex distributions of effective temperature, surface gravity, and type, and by including sub-populations as discussed in Section 6. With a kinematic model, proper motion information would be very informative, especially in terms of differentiating between disc and halo WDs.

When working with real data, there are complications that are not included here but would be straightforward to implement within this framework. Most WD seen by *Gaia* and SDSS are very close to the Sun and almost unaffected by dust. However, hotter and more luminous WDs are seen to further distance and subject to dust reddening and extinction. With a good dust map, selection effects and photometric reddening for such objects can be accounted for. Also not included in this work are incompleteness effects, which are severe for WDs in *Gaia* DR2. This will improve significantly with future DRs, but will still be crucial to account for.

Gaia parallax measurements provide robust identification of WDs, enabling the construction of volume-limited samples, and breaks the degeneracy between distance and size. It is possible to differentiate sub-populations of WDs using this method, such as a population of binary WD systems. Our statistical model fully and correctly accounts for selection effects and observational uncertainties, permitting the construction of a large data sample, without the need to exclude objects with low signal-to-noise ratio or missing parallax information.

ACKNOWLEDGEMENTS

We would like to thank Pierre Bergeron for providing WD atmospheric models with SDSS and *Gaia* passband photometry and the anonymous referee(s) for a constructive review. This work was performed in part at the Aspen Center for Physics, which is supported by National Science Foundation grant PHY-1607611. This work was also partially supported by a grant from the Simons Foundation.

REFERENCES

Althaus L. G., Miller Bertolami M. M., Córsico A. H., 2013, A&A, 557, A19
Ahn C. P. et al., 2012, ApJS, 203, 21
Bergeron P. et al., 2011, ApJ, 737, 28
Bergeron P., Wesemael F., Beauchamp A., 1995, PASP, 107, 1047
Bergeron P., Leggett S. K., Ruiz M. T., 2001, ApJS, 133, 413
Brooks S., Gelman A., Jones G., Meng X.-L., 2011, Handbook of Markov Chain Monte Carlo. CRC Press, Boca Raton, FL
Carrasco J. M., Catalán S., Jordi C., Tremblay P.-E., Napiwotzki R., Luri X., Robin A. C., Kowalski P. M., 2014, A&A, 565, A11
Dame K., Gianninas A., Kilic M., Munn J. A., Brown W. R., Williams K. A., von Hippel T., Harris H. C., 2016, MNRAS, 463, 2453
El-Badry K., Rix H.-W., Weisz D. R., 2018, ApJ, 860, L17
Evans D. W. et al., 2018, A&A, 616, A4
Finley D. S., Koester D., Basri G., 1997, ApJ, 488, 375
Fontaine G., Brassard P., Bergeron P., 2001, PASP, 113, 409
García-Berro E., Oswalt T. D., 2016, New Astron. Rev., 72, 1
Gelman A., Carlin J., Stern H., Dunson D., Vehtari A., Rubin D., 2013, Bayesian Data Analysis, 3rd edn., Chapman and Hall, London
Gentile Fusillo N. P. et al., 2019, MNRAS, 482, 4570
Harris H. C. et al., 2006, AJ, 131, 571
Heavens A., Fantaye Y., Mootoovaloo A., Eggers H., Hosenie Z., Kroon S., Sellentin E., 2017, preprint (arXiv:1704.03472)
Hollands M. A., Tremblay P.-E., Gänsicke B. T., Gentile-Fusillo N. P., Toonen S., 2018, MNRAS, 480, 3942
Isern J., García-Berro E., Hernanz M., Mochkovitch R., Torres S., 1998, ApJ, 503, 239
Istrate A. G., Marchant P., Tauris T. M., Langer N., Stancliffe R. J., Grassitelli L., 2016, A&A, 595, A35
Jiménez-Esteban F. M., Torres S., Rebassa-Mansergas A., Skorobogatov G., Solano E., Cantero C., Rodrigo C., 2018, MNRAS, 480, 4505
Jordan S., 2007, in Napiwotzki R., Burleigh M. R., eds, ASP Conf. Ser. Vol. 372, 15th European Workshop on White Dwarfs, Astron. Soc. Pac., San Francisco, p. 139
Jurić M. et al., 2008, ApJ, 673, 864
Kepler S. O. et al., 2015, MNRAS, 446, 4078
Kepler S. O. et al., 2016, MNRAS, 455, 3413
Kilic M. et al., 2006, AJ, 131, 582
Kilic M., Hambly N. C., Bergeron P., Genest- Beaulieu C., Rowell N., 2018, MNRAS, 479, L113
Kleinman S. J. et al., 2013, ApJS, 204, 5
Koester D., Kepler S. O., 2015, A&A, 583, A86
Li Z., Chen X., Chen H.-L., Han Z., 2018, preprint (arXiv:1812.07226)
Lindegren L. et al., 2018, A&A, 616, A2
Livio M., Mazzali P., 2018, Phys. Rep., 736, 1
Luri X. et al., 2018, A&A, 616, A9
Mestel L., 1952, MNRAS, 112, 583
Metropolis N., Rosenbluth A. W., Rosenbluth M. N., Teller A. H., Teller E., 1953, J. Chem. Phys., 21, 1087
Mortlock D. J., Peiris H. V., Ivezic Z., 2009, MNRAS, 399, 699
Mortlock D. J., Patel M., Warren S. J., Hewett P. C., Venemans B. P., McMahon R. G., Simpson C., 2012, MNRAS, 419, 390
Perryman M. A. C. et al., 1997, A&A, 323, L49
Postnov K. A., Yungelson L. R., 2014, Living Rev. Relativ., 17, 3
Ritossa C., Garcia-Berro E., Iben I., Jr., 1996, ApJ, 460, 489
Smartt S. J., Eldridge J. J., Crockett R. M., Maund J. R., 2009, MNRAS, 395, 1409
Toonen S., Hollands M., Gänsicke B. T., Boekholt T., 2017, A&A, 602, A16
Tremblay P. E., Bergeron P., 2008, ApJ, 672, 1144
Widmark A., Leistedt B., Hogg D. W., 2018, ApJ, 857, 114
Winget D. E., Hansen C. J., Liebert J., van Horn H. M., Fontaine G., Nather R. E., Kepler S. O., Lamb D. Q., 1987, ApJ, 315, L77

This paper has been typeset from a TEX/LATEX file prepared by the author.